



HAL
open science

Warming beneath an East Antarctic ice shelf due to increased subpolar westerlies and reduced sea ice

Julius Lauber, Tore Hattermann, Laura de Steur, Elin Darelius, Matthis Auger, Ole Anders Nøst, Geir Moholdt

► **To cite this version:**

Julius Lauber, Tore Hattermann, Laura de Steur, Elin Darelius, Matthis Auger, et al.. Warming beneath an East Antarctic ice shelf due to increased subpolar westerlies and reduced sea ice. *Nature Geoscience*, 2023, 16 (10), pp.877-885. 10.1038/s41561-023-01273-5 . hal-04287753

HAL Id: hal-04287753

<https://hal.science/hal-04287753>

Submitted on 17 Nov 2023

HAL is a multi-disciplinary open access archive for the deposit and dissemination of scientific research documents, whether they are published or not. The documents may come from teaching and research institutions in France or abroad, or from public or private research centers.

L'archive ouverte pluridisciplinaire **HAL**, est destinée au dépôt et à la diffusion de documents scientifiques de niveau recherche, publiés ou non, émanant des établissements d'enseignement et de recherche français ou étrangers, des laboratoires publics ou privés.



Distributed under a Creative Commons Attribution 4.0 International License





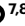
Warming beneath an East Antarctic ice shelf due to increased subpolar westerlies and reduced sea ice

Received: 15 September 2022

Accepted: 17 August 2023

Published online: 21 September 2023

 Check for updates

Julius Lauber ^{1,2}✉, Tore Hattermann ¹, Laura de Steur ¹, Elin Darelius ^{2,3},
Matthis Auger ^{4,5,6}, Ole Anders Nøst ^{7,8} & Geir Moholdt¹

Understanding how climate change influences ocean-driven melting of the Antarctic ice shelves is one of the greatest challenges for projecting future sea level rise. The East Antarctic ice shelf cavities host cold water masses that limit melting, and only a few short-term observational studies exist on what drives warm water intrusions into these cavities. We analyse nine years of continuous oceanographic records from below Fimbulisen and relate them to oceanic and atmospheric forcing. On monthly time scales, warm inflow events are associated with weakened coastal easterlies reducing downwelling in front of the ice shelf. Since 2016, however, we observe sustained warming, with inflowing Warm Deep Water temperatures reaching above 0 °C. This is concurrent with an increase in satellite-derived basal melt rates of 0.62 m yr⁻¹, which nearly doubles the basal mass loss at this relatively cold ice shelf cavity. We find that this transition is linked to a reduction in coastal sea ice cover through an increase in atmosphere–ocean momentum transfer and to a strengthening of remote subpolar westerlies. These results imply that East Antarctic ice shelves may become more exposed to warmer waters with a projected increase of circum-Antarctic westerlies, increasing this region's relevance for sea level rise projections.

The Antarctic ice sheet is a key component of the global climate system^{1,2} and holds enough freshwater to raise global sea level by up to 58 m (refs. 3,4). Basal melting of ice shelves, the floating extensions of the ice sheet, is the main process of mass loss from Antarctica besides iceberg calving^{5–7}. Reduced buttressing⁸ due to ice shelf thinning⁹ is expected to contribute to future sea level rise in a warmer climate¹⁰.

In recent decades, West Antarctic ice shelves have been melting rapidly at rates up to tens of metres per year due to access of 1 °C warm Circumpolar Deep Water beneath the ice¹¹, accounting for most of the net mass loss from the continent. In contrast, the majority of the East Antarctic coast displays an order of magnitude lower melt rates, as

water with temperatures close to the surface freezing point (around –1.8 °C) fills the ice shelf cavities^{6,12}. In particular, the ice shelves in Dronning Maud Land in the Atlantic and Indian sector of the Southern Ocean are shielded by the Antarctic Slope Front (ASF)¹³ from the Warm Deep Water (WDW)¹⁴ that circulates close to the continental shelf break and provides the largest potential heat source for ice shelf melting in this region¹⁵.

Previous studies have found relations between warm inflow and local Ekman dynamics^{16–20}. Still, little is known about the long-term stability of the warm and cold continental shelf regimes²¹, and links between large-scale climate and changes in Antarctic coastal water

¹Norwegian Polar Institute, Tromsø, Norway. ²Geophysical Institute, University of Bergen, Bergen, Norway. ³Bjerknes Centre for Climate Research, Bergen, Norway. ⁴Sorbonne Université, CNRS, LOCEAN, Paris, France. ⁵Institute for Marine and Antarctic studies, University of Tasmania, Hobart, Tasmania, Australia. ⁶The Australian Centre for Excellence in Antarctic Science, University of Tasmania, Hobart, Tasmania, Australia. ⁷Akvaplan-niva AS, Trondheim, Norway. ⁸Oceanbox.io, Tromsø, Norway. ✉e-mail: julius.lauber@npolar.no

mass properties²². Lately, direct WDW access was observed to drive strong ice–ocean interactions in eastern Dronning Maud Land²⁰, and warming of East Antarctic coastal waters has been linked to a poleward shift of the subpolar westerlies²³. Sea ice changes have also been suggested to alter the ASF by modulating the atmosphere–ocean momentum transfer²⁴. Furthermore, circum-Antarctic modelling studies^{25,26} have proposed a teleconnection between warm inflow and remote wind forcing through sea surface height (SSH) anomalies that propagate quickly around the continent^{27,28} and cause onshore bottom Ekman transport anomalies as they weaken the barotropic component of the shelf break current.

For most Antarctic ice shelves, no observations exist that robustly link oceanographic and atmospheric forcing to basal mass loss. Here, we present a unique nine-year-long record of ocean temperature and velocity from below Fimbulisen (FIS), the largest ice shelf in Dronning Maud Land (Fig. 1a). A pivot mooring at the shelf break sill shows that pulses of unmodified WDW enter the ice shelf cavity more frequently after 2016. Analyses of fifth-generation European Centre for Medium-Range Weather Forecasts (ECMWF) reanalysis (ERA5)²⁹, the National Snow and Ice Data Center (NSIDC) sea ice concentration (SIC)³⁰, NSIDC sea ice velocity³¹ and satellite-derived SSH^{32,33} link the warm inflow to increased subpolar westerlies and reduced local sea ice under a more positive Southern Annular Mode (SAM)³⁴. The observed warming of the FIS cavity coincides with an enhanced cavity circulation and anomalously high satellite-derived basal melting³⁵, and the mechanisms revealed by our analyses provide important insights for assessing Antarctic ice shelf stability in a future climate.

Characteristics of warm inflow below FIS

Three sub-ice-shelf moorings with an upper instrument near the ice base and a lower instrument near the sea floor measured temperature and velocity from December 2009 to January 2019 (M1–3; Fig. 1c,d). The lower instrument at mooring M1 (M1_{lower}, at a mean depth of 540 m, roughly 100 m above the bottom) is best suited to capture WDW inflows, being located close to a shelf break sill that connects the FIS cavity with the open ocean^{36,37}. Mooring M2 is located downstream of M1, while mooring M3 is located on a shallower inflow pathway farther east³⁸.

Consistent with the initial two years of the FIS records³⁹, temperatures at M1_{lower} remain within 0.1 °C of the surface freezing point for most of the time (80% of all hourly data), while pulses of warmer water occasionally enter the cavity. However, those pulses intensify after 2016, with 4% (compared with 1% before 2016) of the hourly data exceeding –1.5 °C and unprecedented peak temperatures of 0.2 °C showing unmodified WDW inside the cavity (Fig. 1b). A concurrent warming at M3_{lower} indicates increased access of warmer water also via the shallower sill, while elevated temperatures at M2_{lower} show propagation of WDW further into the cavity along bathymetric contours (Fig. 1c).

A formal regime shift analysis⁴⁰ applied to the monthly mean temperature anomaly and its variance (Methods) confirms the transition in 2016 at all moorings (grey bar in Fig. 1c), while detected shifts

at other times are less robust and more dependent on the parameter choice. For further analyses, we distinguish three periods based on the joint evolution of temperature and velocity over the shelf break sill: two warm periods are apparent at the beginning and the end of the nine-year-long record (Fig. 1c), with monthly background temperatures at or above the surface freezing point and peaks of daily temperatures at M1_{lower} indicating warm intrusions that usually last for one to two days. In contrast, during a cold period between 2013 and 2016 (Fig. 1c), background temperatures largely remain below –1.8 °C and excursions below the surface freezing point at M1_{lower} together with enhanced northward velocities indicate the outflow of ice shelf water⁴¹ across the shelf break sill.

Generally, on shorter time scales, velocities are directed into the cavity during times of higher temperatures (Extended Data Fig. 1a), but also the circulation at the shelf break changed between the three periods (P1–3). During P1, increasing temperatures and southward velocities towards the end of 2010 marked a distinct WDW inflow event. After that, temperature variations decrease, and for the remainder of P1, the filtered velocities only appear as small residuals of the highly variable flow³⁹. During P2, velocities start to oscillate seasonally between inflow in summer and outflow in winter, with a small seasonal imprint on temperature (0.05 °C; Extended Data Fig. 1b). As of mid-2016, increasingly southward velocities and frequent peaks of temperatures indicate a shift towards a more sustained inflow of mWDW (modified WDW, produced by mixing of WDW with shelf water masses) into the cavity during P3.

The weak seasonality in temperature observed at M1_{lower} is in contrast with observations 1,000 km downstream in front of Filchner–Ronne Ice Shelf, where warm inflow^{42–44} is highly seasonal and linked to variations in thermocline depth^{45,46}. Instead, the occurrence of warm intrusions below FIS is dominated by changes on interannual time scales and sub-seasonal fluctuations that have been attributed to internal variability of the ASF³⁹.

Atmospheric forcing associated with warm inflow events

We investigated conditions that promote the access of warm water below FIS by analysing changes in surface pressure and 10 m wind, SIC, ocean stress and ocean stress curl (OSC; Methods), and SSH and geostrophic currents over the course of the mooring observations. Composite maps (Fig. 1e) from one month before warm inflow events (Methods) show that warm events are associated with westerly wind anomalies in front of FIS ($r = 0.36$, maximum at one month lag; Extended Data Fig. 2). These anomalies weaken the persistent easterly winds, which reduces coastal downwelling^{13,18,47} and promotes a shoaling of the ASF, facilitating access of WDW to the cavity. Associated OSC anomalies (Fig. 1f), indicating anomalous open ocean up- or downwelling, show zonal bands of negative anomalies (upwelling) south of 60° S, enhanced along the FIS coast. However, there are no notable trends in local winds (Extended Data Fig. 3), such that these relationships cannot explain why warm inflow events occurred more frequently during P1 and P3.

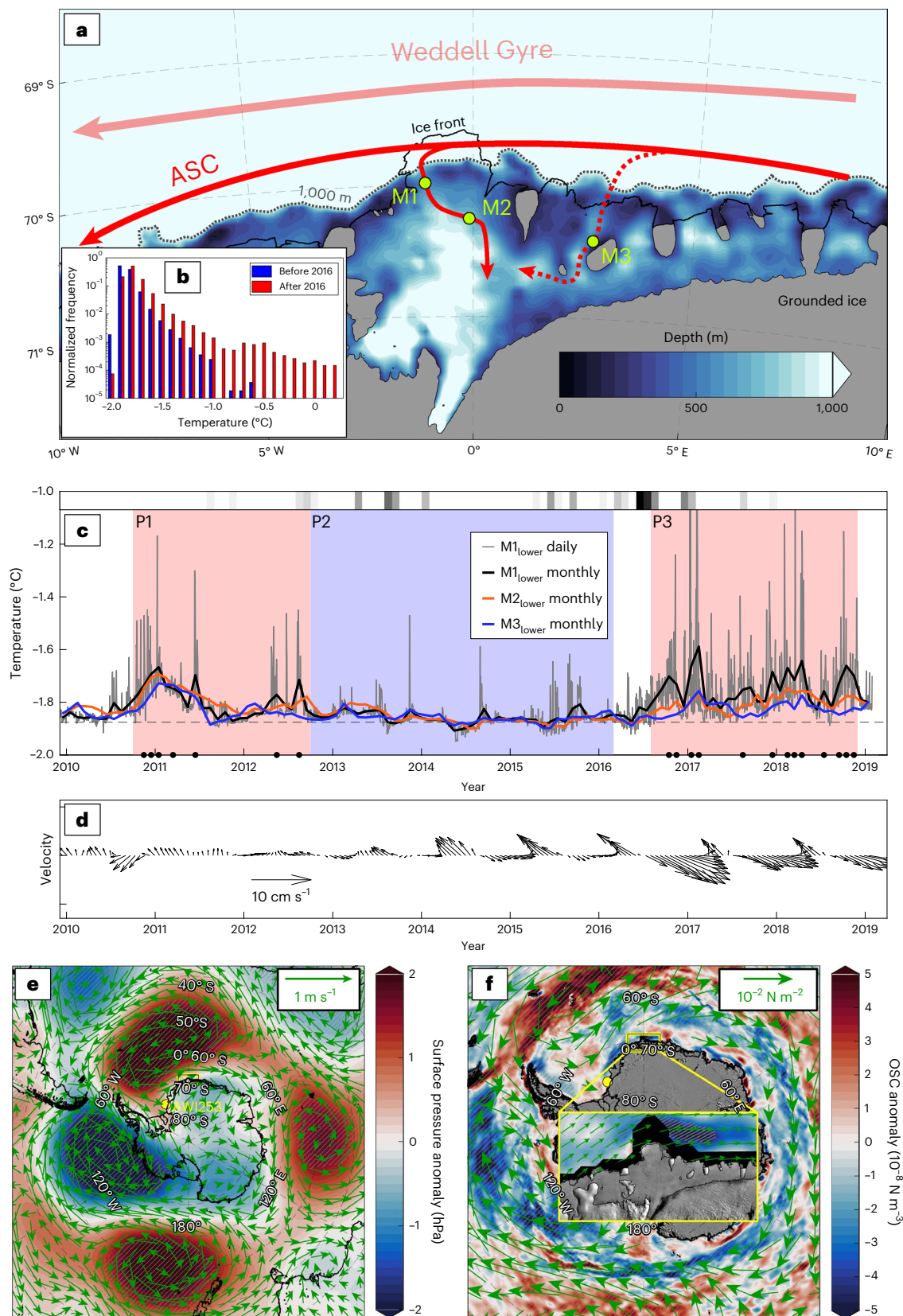
We assessed changes in background conditions (Extended Data Fig. 4) on interannual time scales, based on period mean fields (Fig. 2)

Fig. 1 | Study region, mooring time series and atmospheric forcing. **a**, Map of FIS. Colours show the bathymetry⁷². Green dots show the locations of the three sub-ice-shelf moorings (M1–3). The red arrows indicate the Weddell Gyre and Antarctic Slope Current (ASC), and a main (solid) and secondary (dashed) pathway of mWDW into the FIS cavity. **b**, Histogram comparing the occurrence of M1_{lower} temperatures before and after (including) 2016. The y axis shows the fraction of time before or after 2016, during which the temperature was at the respective bin value. **c**, Monthly mean temperature from the three lower instruments. For M1_{lower}, the daily average is shown additionally. The grey bar shows the timing of shifts in M1–3_{lower} temperature mean and variance detected by a regime shift detection algorithm (colour-coded by frequency of appearance during sensitivity tests, 0 (white)–0.25 (black); Methods), and the coloured

patches indicate warm (red) and cold (blue) periods. The black dots mark months of exceptionally strong warm inflow, as defined in the Methods, and the dashed black line indicates the surface freezing point ($T_f = -1.88$ °C) for a salinity of 34.4 g kg⁻¹. Note that the y axis has been cut off at –1 °C. The maximum temperature is –0.2 °C and occurs in February 2017. **d**, Twenty days binned and 6 bins (= 120 days) filtered vector time series of currents at M1_{lower}. **e**, Anomalies of the 48-month filtered de-seasoned surface pressure and 10 m wind, averaged over the months directly preceding warm inflow events (black dots in **c**). Hatched areas indicate significance for pressure anomalies. The yellow box indicates the location of the study area. **f**, Same as **e**, but for ocean stress and its curl. The satellite image in **f** is from ref. 73.

and time series (Fig. 3 and Extended Data Fig. 5) of relevant dynamical parameters. The atmospheric background state during P1 (Fig. 2a) largely resembles the composite average (Fig. 1e), suggesting that locally weakened coastal easterlies associated with positive surface pressure anomalies in the Atlantic sector of the Southern Ocean were the primary driver for the singular warm inflow event in P1 (Fig. 4a).

In P2 and P3, however, wind anomalies in front of FIS (Fig. 2b,c) were not significant, and another mechanism must have been at play to facilitate the observed shift in 2016. Also, the transient evolution of the M1 currents (Fig. 1d) and the distinct change in background states in SIC, OSC and SSH (Fig. 2) indicate a more intricate interplay during the transition from P2 to P3.



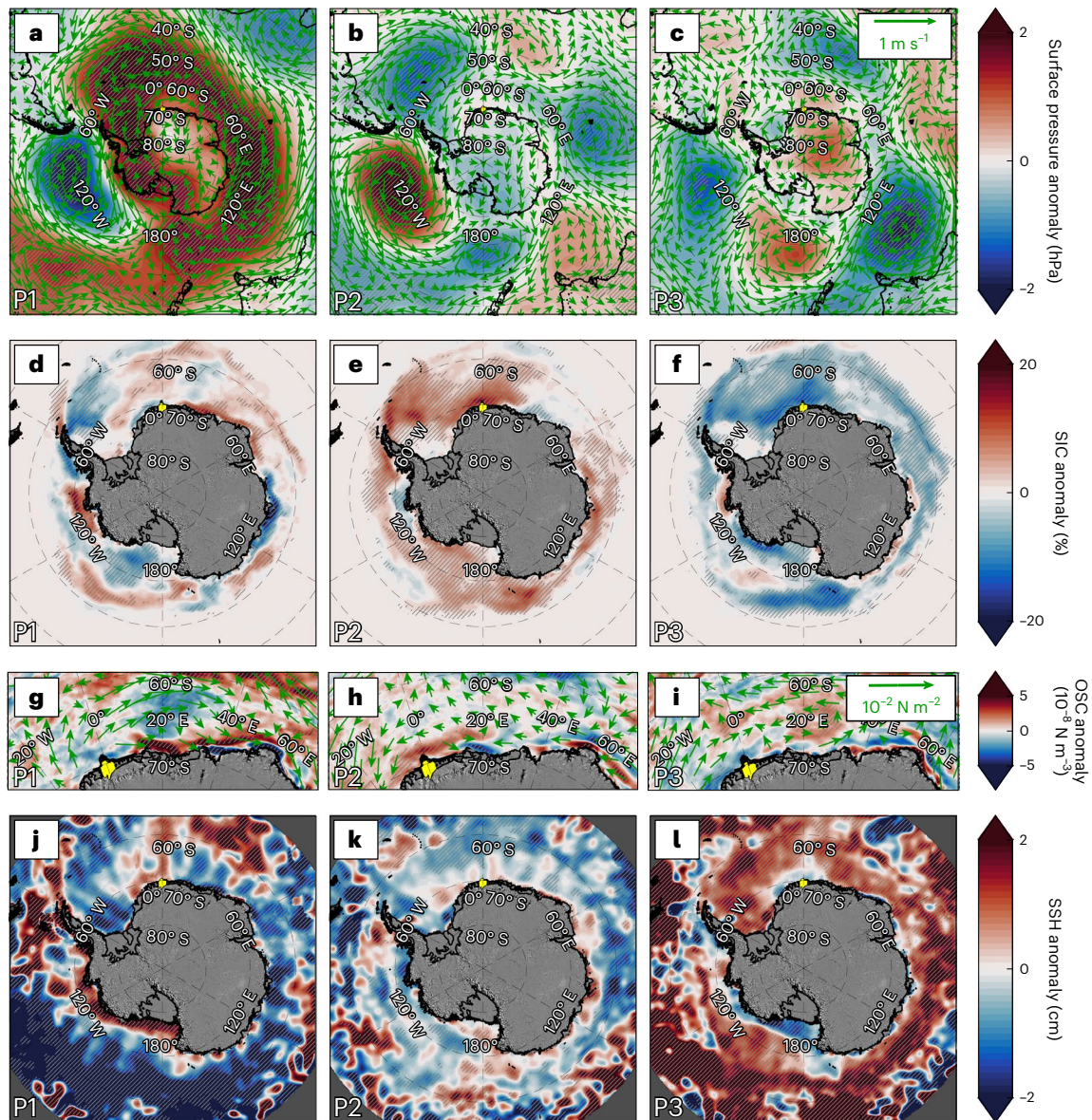


Fig. 2 | Period averages of de-seasoned forcing variables. **a–l**, Surface pressure and wind (**a–c**), SIC (**d–f**), ocean stress and its curl (**g–i**), and SSH (**j–l**) during P1 (left), P2 (centre) and P3 (right). The yellow patches mark the location of FIS.

Hatched areas indicate significance for the properties shown in colour. For reference, the mean states of the variables are shown in Extended Data Fig. 4. The satellite image in **d–l** is from ref. 73.

The role of sea ice and westerlies for warm inflows

The circum-Antarctic reduction in sea ice during P3 (Fig. 2f) is strongest around the southern limb of the Weddell Gyre. Average SIC anomalies in front of FIS change from 1% during P1 and 10% during P2 to -10% during P3 (Fig. 3a). This drop in SIC induced a negative OSC anomaly during P3 by modulating the surface wind stress transfer (Extended Data Fig. 6). Associated open ocean upwelling in the divergence zone⁴⁸ along the East Antarctic coast (Figs. 2i and 3b) counteracts the downwelling of WDW along the coast. Although the OSC anomalies do not correlate significantly with MI_{lower} temperatures (Extended Data Fig. 2), the strengthening of negative OSC before P3 is expected to cause an upward movement of the ASF over the shelf break. The anomalously low SIC in the southern Weddell Gyre may hence have contributed to increased WDW inflow.

In addition to the reduced SIC during P3, the background SSH shows widespread circum-Antarctic anomalies with a band of increased SSH around 60°S and decreased SSH confined along the coast (Fig. 2l).

This pattern differs distinctly from the previous periods, reflecting a weakening of the westward slope current due to the reduction of the meridional SSH gradient at the coast. Modelling studies^{25,26} proposed that such a circum-Antarctic drop in coastal SSH, forced by enhanced subpolar westerlies, promotes warm intrusions to the Antarctic continental shelves via onshore bottom Ekman transport anomalies. If taken as representative of the barotropic component, the average eastward anomaly in geostrophic velocity during P3 (0.6 cm s^{-1}) translates into an onshore bottom Ekman velocity anomaly of 0.2 cm s^{-1} (following ref. 26; Methods). Such Ekman transport anomalies will alter the baroclinic structure of the ASF, and we suggest that the observed changes of the MI_{lower} velocities are indicative of an ASF relaxation that brought WDW closer to the FIS cavity.

The adjustment of SSH and the geostrophic velocity along the East Antarctic shelf break (Fig. 3d,e) started before the transition from P2 to P3, with a drop in SSH and increasingly positive anomalies of the geostrophic velocity from 2015 onwards. Over the same period, velocities

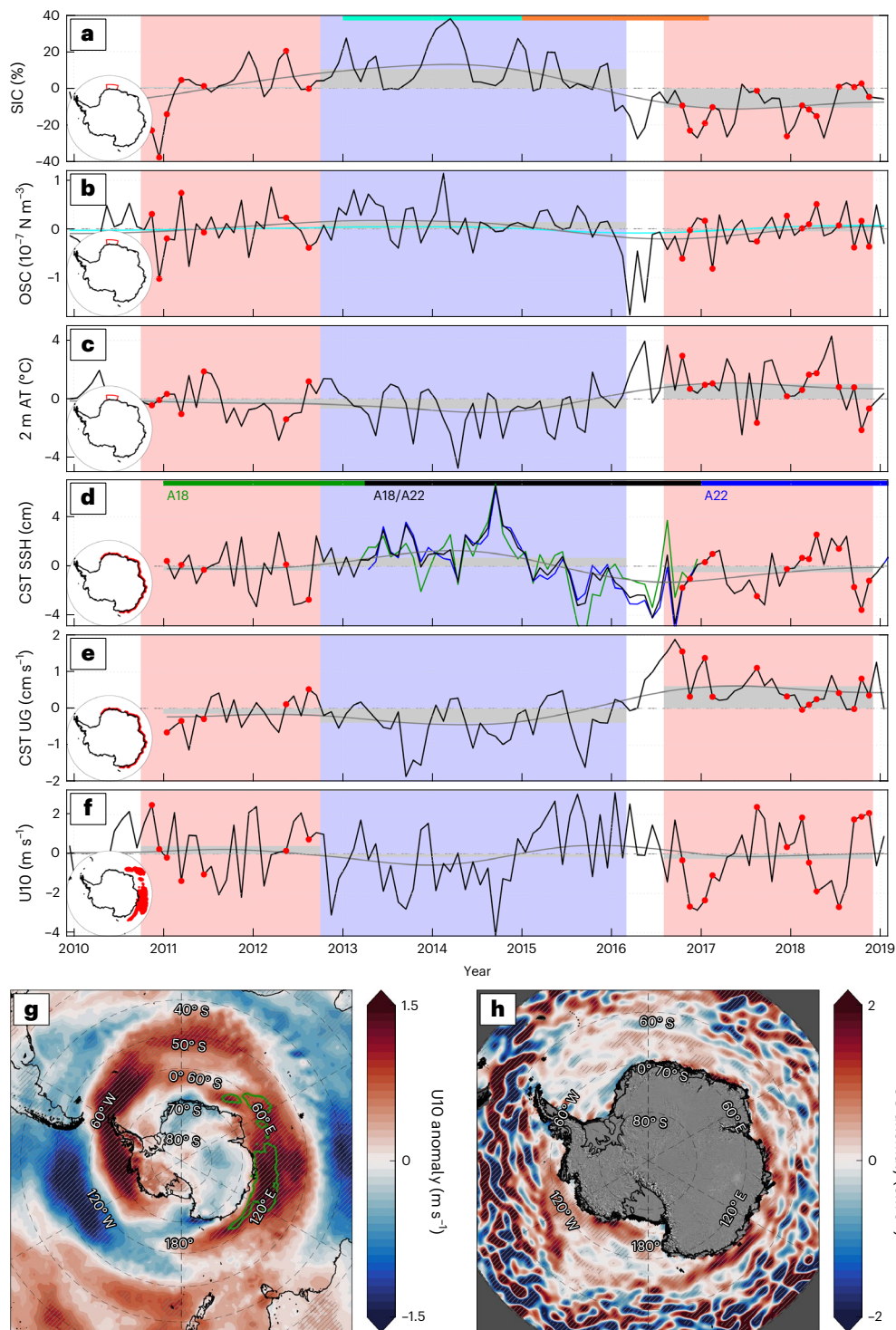


Fig. 3 | Temporal and spatial changes in atmospheric and oceanic forcing. **a–f**, Time series (grey lines are 48-month filtered) of SIC (**a**), OSC (**b**), 2 m air temperature (AT; **c**), coastal (CST) SSH (**d**), coastal zonal geostrophic velocity (CST UG; **e**) and East-Antarctic subpolar 10 m zonal wind (U10; **f**). Insets show maps indicating the area over which the respective time series has been averaged (see Methods for details). The bar in **a** denotes the periods over which the properties in **g–h**, are averaged. The bar in **d** indicates the temporal data coverage and is also valid for **e** (A18: data from ref. 32; A22: data from ref. 33; A18/A22: merged data from both data sets). The green and blue curves show the contributions from both single data sets. The colour patches mark P1–3, as in

Fig. 1c. Grey shadings show the average over P1–3 and red dots mark the values during warm inflow months. The cyan line in **b** is the filtered OSC with seasonally averaged SIC and velocity. For reference, time series of absolute values from **a–f** are shown in Extended Data Fig. 5. **g**, Difference in de-seasoned zonal 10 m wind between 01/2015–01/2017 and 01/2013–12/2014 (orange and cyan bars in **a**, respectively). The green contour marks the areas where the correlation of the coastal SSH (**d**) to the zonal 10 m wind is at least -0.5 (see Extended Data Fig. 7a). Hatched areas indicate significance. **h**, Same as **g**, but for zonal geostrophic velocity. The satellite image in **h** is from ref. 73.

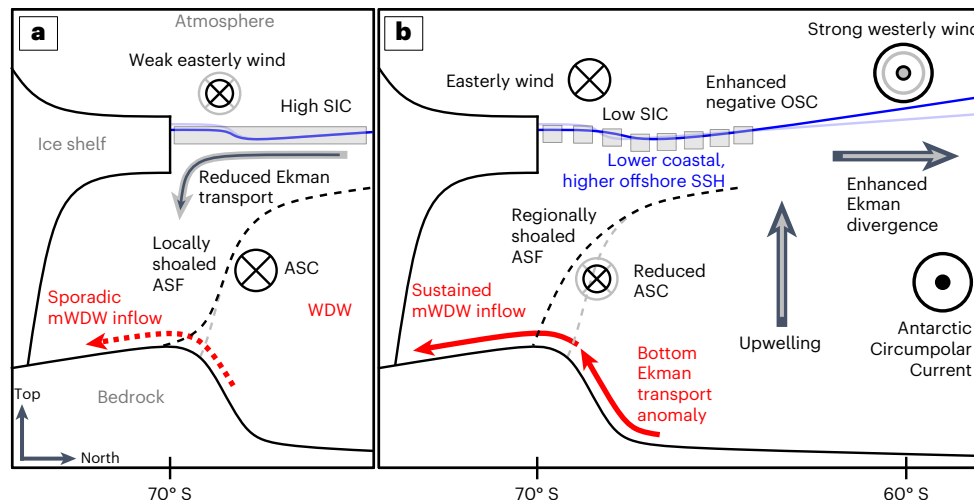


Fig. 4 | Warm inflow mechanisms at FIS. **a**, Local mechanism: weak easterly winds near FIS lead to reduced onshore surface Ekman transport, reduced coastal downwelling and thus a local shoaling of the ASF, resulting in a sporadic inflow of mWDW at depth. **b**, Remote mechanism: anomalously strong subpolar westerlies, associated with negative OSC modulated by less sea ice, result in

enhanced upwelling and northward Ekman transport. Thus, the coastal SSH is anomalously low, and the Antarctic Slope Current (ASC) is weak. This induces anomalous bottom Ekman transport towards the coast, lifting the ASF and facilitating warm inflow. Light grey lines and arrows indicate the background states of the respective processes.

at MI_{lower} show gradually more pronounced seasonal in- and outflows (Fig. 1d), before the onset of the warm inflow when anomalies of SSH (geostrophic velocities) become most negative (positive). Higher temperatures at MI_{lower} correlate weakly with reduced zonal geostrophic velocities on monthly time scales ($r = 0.27$, maximum at four months lag; Extended Data Fig. 2).

The coastal SSH anomalies correlate with the zonal wind (Fig. 3f) and OSC anomalies over a zonal band north of the slope current (maximum at zero lag; Extended Data Fig. 7). Subpolar wind anomalies in a similar region (20–120° E) in numerical simulations^{25,26} implied a causal relationship between the lowering of the circumpolar coastal SSH and an increased circumpolar northward surface Ekman divergence. The differences in winds and geostrophic velocities before and after the period of enhanced westerlies in 2015/16 (Fig. 3g,h) closely resemble the patterns of these simulations: enhanced subpolar westerlies (Fig. 3g) and negative OSC anomalies (upwelling; Extended Data Fig. 8a) cause a decrease in coastal SSH (Extended Data Fig. 8b) and weakening of the slope current (Fig. 3h) that corresponds with the transition to higher temperatures at MI_{lower} in P3 (Fig. 4b). These patterns differ from P1, where minor anomalies in subpolar westerlies (Fig. 3d–f) demonstrate that the remotely forced mechanism is less important than the local short-lived wind anomalies (Figs. 1e and 2a).

Relation to large-scale atmosphere and ocean circulation

The sensitivity to changes in SIC and subpolar westerlies links the access of warmer water below FIS to changes in the large-scale ocean and atmosphere circulation. Because both effects occur simultaneously, it is challenging to quantify their relative contribution to the sustained warm inflow during P3. The distinct SSH anomaly in P3 and similarities to model results of ref. 25 suggest that changes in the circumpolar barotropic mode may have played a central role in the transition to P3. Anomalies in SIC are also significant (Fig. 2f and 3a), but associated OSC anomalies (Fig. 3b) remain relatively small compared with the variability throughout the time series.

The decline in SIC in the Atlantic sector of the Southern Ocean from 2016 onwards has been attributed to anomalous winds near the tip of the Antarctic Peninsula and increased upper ocean temperatures^{49–51} induced by southward atmospheric heat advection⁵². Rising air temperatures (Fig. 3c) in P3 confirm this, while a concurrent peak

in Weddell Gyre strength in 2016⁵³ indicates that increased oceanic heat transport towards the coast may also have contributed to the reduced sea ice cover.

The strength of the subpolar westerlies (Fig. 2f) relates to variations in the SAM ($r = 0.75$)³⁴. Models project that enhanced westerlies under a more positive SAM⁵⁴ will facilitate upwelling of warmer water around Antarctica^{55–57}. In addition, a coherent weakening of the coastal easterlies^{58,59} can enhance the access of WDW to FIS by reducing coastal downwelling, as shown during P1.

Impacts and implications

Our analysis points to a combination of local and remotely forced mechanisms that controls the access of warmer water to the ice shelves in this region of East Antarctica (Fig. 4). Although the mean temperature increase is moderate during the observed warm periods, an intensification of the cavity circulation and anomalies in remote sensing basal melt estimates indicate a direct impact on the ice shelf mass balance. Warm inflow at the main sill is associated with increased velocities at all lower and upper mooring instruments (Fig. 5a,b). This corroborates a stronger overturning inside the cavity from enhanced melt-water input⁶⁰, while an enhanced cavity circulation itself can increase basal melting⁶¹.

Satellite-derived basal melt anomalies³⁵ (Fig. 5c–e; see Extended Data Fig. 9 for mean state and uncertainties) confirm that periods of warmer (colder) water in the cavity are associated with higher (lower) basal melt rates. An increase of basal melting by 0.62 m yr⁻¹ averaged over central FIS (2.5° W–2.5° E) accounts for an additional mass loss of 15.5 Gt yr⁻¹ in P3, nearly doubling the long-term average of 0.67 m yr⁻¹ (16.6 Gt yr⁻¹). Note that melt rates were derived from measured ice shelf height changes after removing the estimated impact from snow accumulation, firn compaction and ice shelf dynamics. Any errors in these components will translate directly into the basal melt rates, and hence the results should be interpreted with care. However, the additional ocean heat flux of 0.15 TW required to sustain the additional mass loss in P3 can realistically be accomplished by the observed temperature anomaly of about 0.2 °C at MI_{lower} in that period (Methods).

Observations downstream of FIS suggest that the transition towards warmer inflows in 2016 is part of a coherent change at larger scales. An exceptionally warm and prolonged flow of mWDW towards Filchner–Ronne Ice Shelf was observed⁶² two months after the strongest

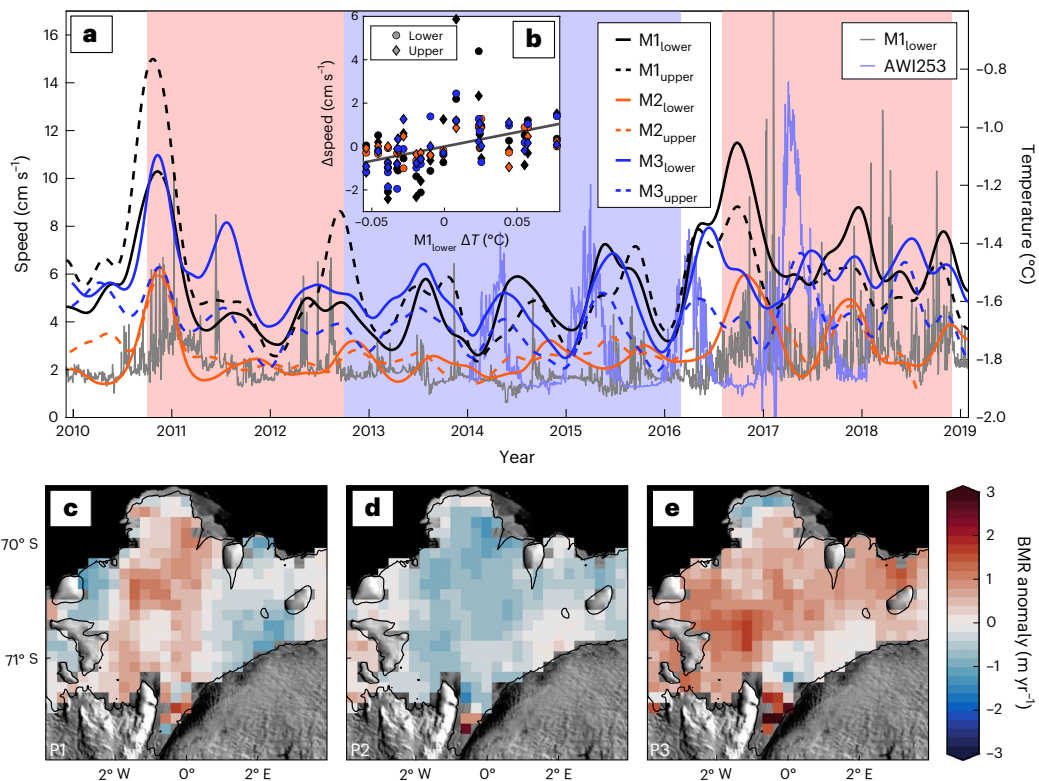


Fig. 5 | Impacts of warm inflow at $M1_{lower}$. **a**, Daily averaged and 180-day low-pass filtered current speed for all mooring instruments (left y axis). For comparison, also the daily averaged $M1_{lower}$ and AWI253 (350 m depth) temperatures are shown (right y axis). **b**, Relation between $M1_{lower}$ temperature and current speed at the six

instruments (see Methods for details). The grey line shows the significant linear trend ($b = 0.13 \text{ m s}^{-1} \text{ } ^\circ\text{C}^{-1}$). **c–e**, Mean de-seasoned basal melt rate (BMR) anomaly of FIS during P1 (**c**), P2 (**d**) and P3 (**e**). Positive (negative) values indicate stronger (weaker) basal melting. The satellite image in **c–e** is from ref. 73.

warm inflow at $M1_{lower}$ in 2017 (mooring AWI253; Fig. 5a). This supports earlier hypotheses of a coherent evolution of the ASF along the East Antarctic margin⁶³, highlighting the role of advection⁶⁴ and associated feedbacks^{46,65,66} for ice shelf basal mass loss around Antarctica.

Direct observations of basal melt rates around 1 m yr^{-1} (ref. 67) at FIS and other ice shelves in Dronning Maud Land^{68,69} are an order of magnitude smaller than melt rates in areas where warm water directly accesses the ice shelf cavities⁶. An increase in the frequency and temperature of warm inflow events—for example, through stronger westerlies⁵⁴ and a weaker coastal current²⁵—may dramatically increase basal mass loss²⁰ and affect ice sheet mass balance in this region¹⁰. This is in line with a recent southward shift of Circumpolar Deep Water along East Antarctica²³, a warming on the southwestern Weddell Sea continental slope after 2019⁷⁰ and high basal melt rates for parts of East Antarctica²⁰. Enhanced basal melting near the ice shelf grounding lines through increased warm inflows at depth will directly affect ice sheet discharge⁹. The links between warm inflows and atmospheric forcing, sea ice and ocean dynamics presented in this study show how climate change may affect basal melting, in addition to more direct effects of atmospheric warming⁷¹. Our East Antarctic cold cavity observations support the remote forcing mechanism proposed by ref. 25, highlighting the role of subpolar westerlies and teleconnections for onshore heat fluxes all around the continent. Hence, large-scale climate dynamics need to be taken into account when assessing future ice sheet stability and sea level rise.

Online content

Any methods, additional references, Nature Portfolio reporting summaries, source data, extended data, supplementary information, acknowledgements, peer review information; details of author contributions and competing interests; and statements of data and code availability are available at <https://doi.org/10.1038/s41561-023-01273-5>.

References

1. Bindshadler, R. Hitting the ice sheets where it hurts. *Science* **311**, 1720–1721 (2006).
2. Garbe, J., Albrecht, T., Levermann, A., Donges, J. F. & Winkelmann, R. The hysteresis of the Antarctic ice sheet. *Nature* **585**, 538–544 (2020).
3. Fretwell, P. et al. Bedmap2: improved ice bed, surface and thickness datasets for Antarctica. *Cryosphere* **7**, 375–393 (2013).
4. Morlighem, M. et al. Deep glacial troughs and stabilizing ridges unveiled beneath the margins of the Antarctic ice sheet. *Nat. Geosci.* **13**, 132–137 (2020).
5. Jacobs, S. S., Hellmer, H. H., Doake, C. S. M., Jenkins, A. & Frolich, R. M. Melting of ice shelves and the mass balance of Antarctica. *J. Glaciol.* **38**, 375–387 (1992).
6. Rignot, E., Jacobs, S., Mouginot, J. & Scheuchl, B. Ice shelf melting around Antarctica. *Science* **341**, 266–270 (2013).
7. Greene, C. A., Gardner, A. S., Schlegel, N.-J. & Fraser, A. D. Antarctic calving loss rivals ice-shelf thinning. *Nature* **609**, 948–953 (2022).
8. Joughin, I., Alley, R. B. & Holland, D. M. Ice-Sheet response to oceanic forcing. *Science* **338**, 1172–1176 (2012).
9. Reese, R., Gudmundsson, G. H., Levermann, A. & Winkelmann, R. The far reach of ice-shelf thinning in Antarctica. *Nat. Clim. Change* **8**, 53–57 (2018).
10. Seroussi, H. et al. ISMIP6 Antarctica: a multi-model ensemble of the Antarctic ice sheet evolution over the 21st century. *Cryosphere* **14**, 3033–3070 (2020).
11. Pritchard, H. D. et al. Antarctic ice-sheet loss driven by basal melting of ice shelves. *Nature* **484**, 502–505 (2012).
12. Thompson, A. F., Stewart, A. L., Spence, P. & Heywood, K. J. The Antarctic Slope Current in a changing climate. *Rev. Geophys.* **56**, 741–770 (2018).

13. Sverdrup, H. U. The currents off the coast of Queen Maud Land. *Nor. Geogr. Tidsskr.* **14**, 239–249 (1954).
14. Nicholls, K. W., Østerhus, S., Makinson, K., Gammelsrød, T. & Fahrbach, E. Ice–ocean processes over the continental shelf of the southern Weddell Sea, Antarctica: a review. *Rev. Geophys.* **47**, RG3003 (2009).
15. Nøst, O. A. et al. Eddy overturning of the Antarctic Slope Front controls glacial melting in the eastern Weddell Sea. *J. Geophys. Res. Oceans* **116**, C11014 (2011).
16. Ohshima, K. I., Takizawa, T., Ushio, S. & Kawamura, T. Seasonal variations of the Antarctic coastal ocean in the vicinity of Lützow-Holm Bay. *J. Geophys. Res. Oceans* **101**, 20617–20628 (1996).
17. Thoma, M., Jenkins, A., Holland, D. & Jacobs, S. Modelling Circumpolar Deep Water intrusions on the Amundsen Sea continental shelf, Antarctica. *Geophys. Res. Lett.* **35**, L18602 (2008).
18. Smedsrud, L. H., Jenkins, A., Holland, D. M. & Nøst, O. A. Modeling ocean processes below Fimbulisen, Antarctica. *J. Geophys. Res. Oceans* **111**, C01007 (2006).
19. Assmann, K. M., Darelius, E., Wåhlin, A. K., Kim, T. W. & Lee, S. H. Warm Circumpolar Deep Water at the western Getz Ice Shelf front, Antarctica. *Geophys. Res. Lett.* **46**, 870–878 (2019).
20. Hirano, D. et al. Strong ice–ocean interaction beneath Shirase Glacier Tongue in East Antarctica. *Nat. Commun.* **11**, 4221 (2020).
21. Petty, A. A., Feltham, D. L. & Holland, P. R. Impact of atmospheric forcing on Antarctic continental shelf water masses. *J. Phys. Oceanogr.* **43**, 920–940 (2013).
22. Jourdain, N. C. et al. A protocol for calculating basal melt rates in the ISMIP6 Antarctic ice sheet projections. *Cryosphere* **14**, 3111–3134 (2020).
23. Herraiz-Borreguero, L. & Naveira Garabato, A. C. Poleward shift of Circumpolar Deep Water threatens the East Antarctic Ice Sheet. *Nat. Clim. Change* **12**, 728–734 (2022).
24. Núñez-Riboni, I. & Fahrbach, E. Seasonal variability of the Antarctic Coastal Current and its driving mechanisms in the Weddell Sea. *Deep Sea Res. I* **56**, 1927–1941 (2009).
25. Spence, P. et al. Localized rapid warming of West Antarctic subsurface waters by remote winds. *Nat. Clim. Change* **7**, 595–603 (2017).
26. Webb, D. J., Holmes, R. M., Spence, P. & England, M. H. Barotropic Kelvin wave-induced bottom boundary layer warming along the West Antarctic Peninsula. *J. Geophys. Res. Oceans* **124**, 1595–1615 (2019).
27. Webb, D. J., Holmes, R. M., Spence, P. & England, M. H. Propagation of barotropic Kelvin waves around Antarctica. *Ocean Dyn.* **72**, 405–419 (2022).
28. Auger, M., Sallée, J.-B., Prandi, P. & Naveira Garabato, A. C. Subpolar Southern Ocean seasonal variability of the geostrophic circulation from multi-mission satellite altimetry. *J. Geophys. Res. Oceans* **127**, e2021JC018096 (2022).
29. Hersbach, H. et al. *ERA5 Monthly Averaged Data on Single Levels from 1979 to Present* (Copernicus Climate Change Service (C3S) Climate Data Store (CDS), 2019); <https://doi.org/10.24381/cds.f17050d7>
30. Cavalieri, D. J., Parkinson, C. L., Gloersen, P. & Zwally, H. J. *Sea Ice Concentrations from Nimbus-7 SMMR and DMSP SSM/I-SSMIS Passive Microwave Data, Version 1* (NASA National Snow and Ice Data Center Distributed Active Archive Center, 1996); <https://doi.org/10.5067/8GQ8LZQVLOVL>
31. Tschudi, M., Meier, W. N., Stewart, J. S., Fowler, C. & Maslanik, J. *Polar Pathfinder Daily 25 km EASE-Grid Sea Ice Motion Vectors, Version 4* (NASA National Snow and Ice Data Center Distributed Active Archive Center, 2019); <https://doi.org/10.5067/INAWUWO7QH7B>
32. Armitage, T. W. K., Kwok, R., Thompson, A. F. & Cunningham, G. Dynamic topography and sea level anomalies of the Southern Ocean: variability and teleconnections. *J. Geophys. Res. Oceans* **123**, 613–630 (2018).
33. Auger, M., Prandi, P. & Sallée, J.-B. Southern Ocean sea level anomaly in the sea ice-covered sector from multimission satellite observations. *Sci. Data* **9**, 70 (2022).
34. Marshall, G. J. Trends in the Southern Annular Mode from observations and reanalyses. *J. Climate* **16**, 4134–4143 (2003).
35. Adusumilli, S., Fricker, H. A., Medley, B., Padman, L. & Siegfried, M. R. Interannual variations in meltwater input to the Southern Ocean from Antarctic ice shelves. *Nat. Geosci.* **13**, 616–620 (2020).
36. Nøst, O. A. Measurements of ice thickness and seabed topography under the Fimbul Ice Shelf, Dronning Maud Land, Antarctica. *J. Geophys. Res. Oceans* **109**, C10010 (2004).
37. Nicholls, K. W., Abrahamsen, E. P., Heywood, K. J., Stansfield, K. & Østerhus, S. High-latitude oceanography using the Autosub autonomous underwater vehicle. *Limnol. Oceanogr.* **53**, 2309–2320 (2008).
38. Nicholls, K. W. et al. Measurements beneath an Antarctic ice shelf using an autonomous underwater vehicle. *Geophys. Res. Lett.* **33**, L08612 (2006).
39. Hattermann, T., Nøst, O. A., Lilly, J. M. & Smedsrud, L. H. Two years of oceanic observations below the Fimbul Ice Shelf, Antarctica. *Geophys. Res. Lett.* **39**, L12605 (2012).
40. Rodionov, S. N. A sequential algorithm for testing climate regime shifts. *Geophys. Res. Lett.* **31**, L09204 (2004).
41. Foldvik, A. et al. Ice shelf water overflow and bottom water formation in the southern Weddell Sea. *J. Geophys. Res. Oceans* **109**, C02015 (2004).
42. Årthun, M., Nicholls, K. W., Makinson, K., Fedak, M. A. & Boehme, L. Seasonal inflow of warm water onto the southern Weddell Sea continental shelf, Antarctica. *Geophys. Res. Lett.* **39**, L17601 (2012).
43. Darelius, E., Fer, I. & Nicholls, K. W. Observed vulnerability of Filchner–Ronne Ice Shelf to wind-driven inflow of Warm Deep Water. *Nat. Commun.* **7**, 12300 (2016).
44. Ryan, S., Hattermann, T., Darelius, E. & Schröder, M. Seasonal cycle of hydrography on the eastern shelf of the Filchner Trough, Weddell Sea, Antarctica. *J. Geophys. Res. Oceans* **122**, 6437–6453 (2017).
45. Semper, S. & Darelius, E. Seasonal resonance of diurnal coastal trapped waves in the southern Weddell Sea, Antarctica. *Ocean Sci.* **13**, 77–93 (2017).
46. Hattermann, T. Antarctic thermocline dynamics along a narrow shelf with easterly winds. *J. Phys. Oceanogr.* **48**, 2419–2443 (2018).
47. Nakayama, Y. et al. Antarctic Slope Current modulates ocean heat intrusions towards Totten Glacier. *Geophys. Res. Lett.* **48**, e2021GL094149 (2021).
48. Hayakawa, H., Shibuya, K., Aoyama, Y., Nogi, Y. & Doi, K. Ocean bottom pressure variability in the Antarctic Divergence Zone off Lützow-Holm Bay, East Antarctica. *Deep Sea Res. I* **60**, 22–31 (2012).
49. Turner, J. et al. Unprecedented springtime retreat of Antarctic sea ice in 2016. *Geophys. Res. Lett.* **44**, 6868–6875 (2017).
50. Meehl, G. A. et al. Sustained ocean changes contributed to sudden Antarctic sea ice retreat in late 2016. *Nat. Commun.* **10**, 14 (2019).
51. Turner, J. et al. Recent decrease of summer sea ice in the Weddell Sea, Antarctica. *Geophys. Res. Lett.* **47**, e2020GL087127 (2020).
52. Schlosser, E., Haumann, F. A. & Raphael, M. N. Atmospheric influences on the anomalous 2016 Antarctic sea ice decay. *Cryosphere* **12**, 1103–1119 (2018).

53. Neme, J., England, M. H. & Hogg, A. M. Seasonal and interannual variability of the Weddell Gyre from a high-resolution global ocean-sea ice simulation during 1958–2018. *J. Geophys. Res. Oceans* **126**, e2021JC017662 (2021).
54. Zheng, F., Li, J., Clark, R. T. & Nnamchi, H. C. Simulation and projection of the Southern Hemisphere Annular Mode in CMIP5 models. *J. Climate* **26**, 9860–9879 (2013).
55. Fyfe, J. C., Saenko, O. A., Zickfeld, K., Eby, M. & Weaver, A. J. The role of poleward-intensifying winds on Southern Ocean warming. *J. Climate* **20**, 5391–5400 (2007).
56. Spence, P. et al. Rapid subsurface warming and circulation changes of Antarctic coastal waters by poleward shifting winds. *Geophys. Res. Lett.* **41**, 4601–4610 (2014).
57. Verfaillie, D. et al. The circum-Antarctic ice-shelves respond to a more positive Southern Annular Mode with regionally varied melting. *Commun. Earth Environ.* **3**, 139 (2022).
58. Bracegirdle, T. J., Connolley, W. M. & Turner, J. Antarctic climate change over the twenty first century. *J. Geophys. Res. Atmos.* **113**, D03103 (2008).
59. Neme, J., England, M. H. & Hogg, A. M. Projected changes of surface winds over the Antarctic continental margin. *Geophys. Res. Lett.* **49**, e2022GL098820 (2022).
60. Jourdain, N. C. et al. Ocean circulation and sea-ice thinning induced by melting ice shelves in the Amundsen Sea. *J. Geophys. Res. Oceans* **122**, 2550–2573 (2017).
61. Jenkins, A., Nicholls, K. W. & Corr, H. F. J. Observation and parameterization of ablation at the base of Ronne Ice Shelf, Antarctica. *J. Phys. Oceanogr.* **40**, 2298–2312 (2010).
62. Ryan, S. et al. Exceptionally warm and prolonged flow of warm deep water toward the Filchner–Ronne Ice Shelf in 2017. *Geophys. Res. Lett.* **47**, e2020GL088119 (2020).
63. Le Pailh, N. et al. Coherent seasonal acceleration of the Weddell Sea boundary current system driven by upstream winds. *J. Geophys. Res. Oceans* **125**, e2020JC016316 (2020).
64. Graham, J. A., Heywood, K. J., Chavanne, C. P. & Holland, P. R. Seasonal variability of water masses and transport on the Antarctic continental shelf and slope in the southeastern Weddell Sea. *J. Geophys. Res. Oceans* **118**, 2201–2214 (2013).
65. Bronselaer, B. et al. Change in future climate due to Antarctic meltwater. *Nature* **564**, 53–58 (2018).
66. Bull, C. Y. S. et al. Remote control of Filchner–Ronne Ice Shelf melt rates by the Antarctic Slope Current. *J. Geophys. Res. Oceans* **126**, e2020JC016550 (2021).
67. Langley, K. et al. Low melt rates with seasonal variability at the base of Fimbul Ice Shelf, East Antarctica, revealed by in situ interferometric radar measurements. *Geophys. Res. Lett.* **41**, 8138–8146 (2014).
68. Sun, S. et al. Topographic shelf waves control seasonal melting near Antarctic ice shelf grounding lines. *Geophys. Res. Lett.* **46**, 9824–9832 (2019).
69. Lindbäck, K. et al. Spatial and temporal variations in basal melting at Nivlisen Ice Shelf, East Antarctica, derived from phase-sensitive radars. *Cryosphere* **13**, 2579–2595 (2019).
70. Darelius, E., Dundas, V., Janout, M. & Tippenhauer, S. Sudden, local temperature increase above the continental slope in the southern Weddell Sea, Antarctica. *Ocean Sci.* **19**, 671–683 (2023).
71. Kusahara, K. & Hasumi, H. Modeling Antarctic ice shelf responses to future climate changes and impacts on the ocean. *J. Geophys. Res. Oceans* **118**, 2454–2475 (2013).
72. Eisermann, H., Eagles, G., Ruppel, A., Smith, E. C. & Jokat, W. *Bathymetry Beneath Ice Shelves of Western Dronning Maud Land, East Antarctica* (PANGAEA, 2020); <https://doi.org/10.1594/PANGAEA.913742>
73. Haran, T. et al. *MEaSURES MODIS Mosaic of Antarctica 2013-2014 (MOA2014) Image Map, Version 1* (NASA National Snow and Ice Data Center Distributed Active Archive Center, 2019); <https://doi.org/10.5067/RNF17BP824UM>

Publisher's note Springer Nature remains neutral with regard to jurisdictional claims in published maps and institutional affiliations.

Open Access This article is licensed under a Creative Commons Attribution 4.0 International License, which permits use, sharing, adaptation, distribution and reproduction in any medium or format, as long as you give appropriate credit to the original author(s) and the source, provide a link to the Creative Commons license, and indicate if changes were made. The images or other third party material in this article are included in the article's Creative Commons license, unless indicated otherwise in a credit line to the material. If material is not included in the article's Creative Commons license and your intended use is not permitted by statutory regulation or exceeds the permitted use, you will need to obtain permission directly from the copyright holder. To view a copy of this license, visit <http://creativecommons.org/licenses/by/4.0/>.

© The Author(s) 2023

Methods

Ice shelf moorings

The three oceanic sub-ice-shelf moorings (M1–3; Fig. 1a) were initially deployed below FIS during a hot-water-drilling campaign in 2009/10, intended to provide data for about five years based on the expected lifetime of the instruments. However, all batteries and data storage units at the ice shelf surface are replaceable, such that the system can be maintained ad infinitum, as long as there is no hardware failure. After initial ground-based yearly data retrieval and battery replacements in 2010/11 and 2012/13, a two-yearly air-supported service interval was adopted until the onset of the worldwide COVID-19 pandemic prohibited access to the sites in 2020/21.

Hourly temperature and velocity data from the moorings are available until January 2019. Each of the moorings is equipped with two Aanderaa RCM9 current meter instruments, an upper one close to the ice base and a lower one close to the seabed³⁹. Owing to strong sensor drift, the conductivity (and therefore also salinity) data have been discarded. The moorings are hanging from the ice shelf, and are hence advected with the floating ice as it advances. Between 2009 and 2019, M1 and M2 both moved about 6 km north–northwest, while M3 moved less than 500 m. It is possible that the temperature increase observed at M1_{lower} during P3 is the result of the mooring being advected closer to the shelf break and the ASF, but as a warming is observed also at M2/3_{lower} during the same period, this explanation is not plausible.

Although mooring instrumentation recorded at hourly intervals, we here use daily or monthly mean values⁷⁴. The records are de-seasoned to obtain interannual monthly anomalies, that is, for each monthly value, the average over the corresponding months in the record is subtracted. Times of exceptionally strong warm inflow are then defined as the months during which the de-seasoned M1_{lower} temperature exceeds one standard deviation (black dots in Fig. 1c). The three periods are P1: 10/2010–09/2012; P2: 10/2012–02/2016; P3: 08/2016–11/2018. Months at the edges of these periods that cannot distinctly be assigned to the warm or cold periods are left out of this classification. Results based on the period classification are not sensitive to the exact temporal definition of P1–3. Also, the P1–3 distinction is consistent when examining each year and the seasonal variability of each year, as the interannual variability of the M1_{lower} temperature and most forcing variables exceed their respective mean seasonal cycle (Extended Data Fig. 5).

Auxiliary data sets

Monthly 2 m air temperature, surface pressure and 10 m wind data with 0.25° spatial resolution are obtained from ERA5 reanalysis²⁹, daily passive microwave SIC data from NSIDC³⁰ and daily sea ice velocity data, also from NSIDC³¹, both with 25 km spatial resolution.

Monthly SSH data, derived from satellite altimetry and covering the period from January 2011 to December 2016, are obtained from ref. 32 (A18 hereafter), and combined with a newer daily product from ref. 33 (A22 hereafter), covering the period from April 2013 to July 2019. The data sets have been obtained using different methods, so they are not expected to be exactly the same. For A22, the same 300 km low-pass filter as in its validation process is applied, in order to reach a spatial smoothness consistent with the one in A18. Because the A22 data consist of SSH anomalies rather than absolute values, some steps are undertaken to bring both data sets to a comparable level. The A18 data are interpolated on the A22 grid. The respective temporal mean during the overlapping period of both data sets (April 2013 to December 2016) of the anomaly to the whole period mean is subtracted from each data set. To also have the A22 data as absolute SSH values, the mean A18 SSH is added to these. After that, during their overlapping time, both data sets compare reasonably well, with the A18 SSH being on average 0.03 mm higher. Finally, the data sets are monthly merged in time. During the overlapping period, the average between both data sets for each data point is taken. Note that, as shown by ref. 33, processing only

CryoSat-2 measurements for the development of a gridded SSH data set may create a sampling bias in the subpolar Southern Ocean, resulting in an artificial meridional stripe pattern. This is the case in the data from ref. 32 and may impact parts of our combined SSH data. From the combined SSH data, geostrophic velocities are calculated according to:

$$\mathbf{u}_{\text{geo}} = \frac{g}{f} (\mathbf{k} \times \nabla \text{SSH}) \quad (1)$$

where $g = 9.81 \text{ m s}^{-2}$ is the gravitational acceleration, f is the Coriolis parameter, $\mathbf{k} = (001)^T$ is the unity vector in the third dimension and $\nabla = (\partial/\partial x \partial/\partial y \partial/\partial z)^T$ is the nabla differential operator.

The monthly SAM index was downloaded from <https://legacy.bas.ac.uk/met/gjima/sam.html>. It is defined as the difference in mean sea level pressure between six stations around 40° S and six stations around 65° S, spread over a wide range of longitudes³⁴. Thus, positive (negative) values indicate stronger (weaker) than normal subpolar circum-Antarctic westerlies.

Data from mooring AWI253 are available from refs. 75 and 76, and have been previously analysed in ref. 62.

From wind, SIC and ice velocity, the ocean stress is calculated following refs. 77 and 78:

$$\boldsymbol{\tau} = \alpha \boldsymbol{\tau}_{\text{ice-water}} + (1 - \alpha) \boldsymbol{\tau}_{\text{air-water}} \quad (2)$$

where

$$\boldsymbol{\tau}_{\text{ice-water}} = \rho_w C_{\text{iw}} |\mathbf{U}_i| \mathbf{U}_i \quad (3)$$

$$\boldsymbol{\tau}_{\text{air-water}} = \rho_a C_d |\mathbf{U}_a| \mathbf{U}_a \quad (4)$$

where α is SIC, $\rho_a = 1.25 \text{ kg m}^{-3}$ is the density of air, $\rho_w = 1,028 \text{ kg m}^{-3}$ is the density of seawater, \mathbf{U}_i is the horizontal sea ice velocity, \mathbf{U}_a is the 10 m horizontal wind and $C_d = 1.25 \times 10^{-3}$ and $C_{\text{iw}} = 5.50 \times 10^{-3}$ (ref. 79) are the drag coefficients for the air–water and ice–water interface, respectively. Ocean currents are neglected in the calculation because they are assumed to be orders of magnitude weaker than the wind. The curl of this ocean stress is then calculated as:

$$\text{OSC} = (\mathbf{k} \times \nabla) \cdot \boldsymbol{\tau} = \frac{\partial \tau_y}{\partial x} - \frac{\partial \tau_x}{\partial y} \quad (5)$$

where $\mathbf{k} = (001)^T$ is the unity vector in the third dimension. By a factor of the inverse product of Coriolis parameter and density, the OSC is then proportional to Ekman pumping. In the Southern Hemisphere, a positive OSC thus induces Ekman downwelling, and a negative OSC Ekman upwelling. Note that the OSC does not include coastal downwelling due to onshore Ekman transport, because the ice shelf as a physical boundary is not included in the calculation.

Time series of basal melt rates for FIS are calculated using data from ref. 35 according to their equation (7):

$$w_b(t) = \frac{M_s}{\rho_i} - \frac{\rho_w}{\rho_w - \rho_i} \left(\frac{dh}{dt} - \frac{dh_{\text{air}}}{dt} \right) \quad (6)$$

where M_s is the surface mass balance, $\rho_i = 917 \text{ kg m}^{-3}$ is the density of ice, $\rho_w = 1,028 \text{ kg m}^{-3}$ is the density of seawater, h is the ice shelf surface height relative to the ocean surface and h_{air} is the firn air content. These data are available at a three-monthly resolution and taken from December 2009 to November 2018. Uncertainties for the single values of the basal melt rates are calculated according to Gauss' law of error propagation:

$$(\sigma_{w_b})_{\text{single}} = \sqrt{\left(\frac{\partial w_b}{\partial h} \right)^2 \sigma_h^2 + \left(\frac{\partial w_b}{\partial h_{\text{air}}} \right)^2 \sigma_{h_{\text{air}}}^2} \quad (7)$$

where w_b is taken from equation (6), σ_h and $\sigma_{h_{air}}$ are independent of each other and constant in time, and uncertainties for h and h_{air} are given in ref. 35. Uncertainties in the period averages of the basal melt rates (Fig. 5c–e) are then calculated as:

$$(\sigma_{w_b})_{avg} = \frac{1}{\sqrt{n}}(\sigma_{w_b})_{single} \quad (8)$$

where n is the number of three-monthly basal melt rate values within a period, that is, 8, 14 and 10 for P1–3, respectively. Note that uncertainties of h and h_{air} are not given for every grid point where h and h_{air} are given, leading to missing uncertainties for w_b at the edges of FIS. The results of the calculation are shown in Extended Data Fig. 9b–d.

Data analysis

A sequential regime shift detection algorithm⁴⁰ was applied to our temperature time series to examine the significance of enhanced warm inflows after 2016. This method tests if a change in mean value during a specified window length is significant according to a Student's t -test⁸⁰, based on the assumption that the variance of the time series does not change with time. For this purpose, the probability density function of the input time series must be normalized. In addition to an increase in mean temperature, a characteristic change in P3 is the more frequent occurrence of short-lived warm pulses (Fig. 1c), which appears as a long tail in the temperature distribution (Fig. 1b), without necessarily affecting the mean value of the period. Hence, in addition to applying the method to the temperature time series itself, we use an additional measure to describe the change in time of the temperature distribution, defined as the variance of the incremental difference between two successive hourly values computed for monthly intervals, hereafter referred to as incremental variance. Describing the amount of variability within each month with a scalar value, the probability density function of the incremental variance time series was normalized and used as an input for the regime shift detection algorithm.

Although the detected shifts in our time series are sensitive to the window length and the significance threshold of the algorithm, the transition in 2016 stands out as a robust feature for various parameter choices. To illustrate this, we computed an ensemble of detected shifts based on the monthly de-seasoned temperature time series from all three lower mooring instruments and their incremental variance. For each of these six time series, the window length (2, 3, 5, 8 years) and the significance threshold (0.01, 0.1, 1, 2, 5, 10%) are varied, giving in total $6 \times 4 \times 6 = 144$ ensemble members. The grey shaded bar in Fig. 1c shows the fraction of ensemble members that detect a regime shift in a specific month, with darker colours indicating regime shift detected by a larger number of ensemble members.

All auxiliary data records, except the SAM index, were de-seasoned. This ensures that any feature observed in these data is unrelated to seasonality. To correct for any long-term features within the de-seasoned data, the event-based composites in Fig. 1e,f are calculated using a 48-month high-pass filter. The correlation between the MI_{lower} temperature record and the local wind is highest for a lag of one month, and hence a one-month lag was applied when making the composites. The correlation is insignificant for zero lag (Extended Data Fig. 2). We test the significance of composite means using a Monte Carlo approach, that is, by testing 1,000 times for each variable and each spatial data point if a positive (negative) average value is larger (smaller) than the average value during the same amount of, but randomly selected, months within the mooring period. If this is the case for at least 95% of the conducted tests, the composite signal at that occasion is defined as significant. The significance of correlations is calculated using a two-sided t -test. The t -value is:

$$t = r\sqrt{\frac{n-2}{1-r^2}} \quad (9)$$

where r is the correlation coefficient between two time series and n is their number of effective degrees of freedom. The significance is then:

$$\text{sig} = 1 - 2 \text{tcdf}(-|t|, n - 2) \quad (10)$$

where tcdf is the cumulative density function of Student's t -distribution⁸⁰. The significance threshold is taken as 95%.

Time series in Fig. 3a–c are averaged over an upstream area close to FIS (5° W–15° E and 70° S–67° S), due to a potential influence from the prevailing easterly winds and westward currents. The coastal SSH and geostrophic velocity anomalies in Fig. 3d,e are averaged over 20° W to 160° E, with two additional criteria of (1) being at maximum 50 km away from the coast based on coastline data from ref. 81; and (2) the bathymetry not being deeper than 2,000 m based on Bedmap2 topographic data from ref. 3. These choices are made to confine the average to data points over a narrow continental shelf. The wide longitudinal range of the averages is chosen due to a coherent eastward coastal current, with barotropic anomalies quickly propagating along the convex perimeter of the continent²⁷. The averages in Fig. 3d,e are thus not sensitive to the choice of the bounding longitudes. The subpolar wind anomaly in Fig. 3f is averaged over the area where the correlation of the zonal 10 m wind to the coastal SSH anomaly is at least -0.5 .

The magnitude of the bottom Ekman velocity anomaly during P3 is estimated from equations (8)–(10) from ref. 26. Assuming no continental slope in the zonal direction and a negligible meridional anomaly of the barotropic coastal current, the southward magnitude of the bottom Ekman velocity anomaly is:

$$|u'_e| = \frac{\overline{U'_{P3}}}{A} \quad (11)$$

where $\overline{U'_{P3}} = 0.6 \text{ cm s}^{-1}$ is the mean anomaly of the zonal geostrophic coastal current during P3, that is, the value of the right black shading in Fig. 3e, and $A = \pi$ is a parameter for the effective thickness of the bottom Ekman layer. This gives a mean bottom Ekman velocity anomaly of $|u'_e| = 0.2 \text{ cm s}^{-1}$ during P3.

In Fig. 5b, the daily temperature of MI_{lower} and current speeds from all six instruments have been low-pass median-filtered over 48 days and afterwards binned on time intervals of 180 days before conducting the linear regression. The anomalies of temperature and current speeds are calculated with respect to the mean of the respective device over the whole mooring period. A significance test of the trend is conducted by shuffling the current speeds 1,000 times, calculating each linear trend, and counting how often the observed trend lies above the randomly created ones. Again, if this is the case for at least 95% of the tests, the trend is taken as significant.

The mass loss rate of FIS is calculated as:

$$\Delta m = \rho_i \Delta x \Delta y \sum_{2.5^\circ \text{ E}}^{2.5^\circ \text{ W}} \overline{B_{P3}} \quad (12)$$

where $\rho_i = 917 \text{ kg m}^{-3}$ is the density of ice, $\Delta x = \Delta y = 10 \text{ km}$ are the side lengths of a grid cell and $\overline{B_{P3}}$ are the mean de-seasoned basal melt rates during P3 (Fig. 5e). The longitudes under and over the sum sign indicate the zonal extent over which the calculation is done. Meridionally, the whole extent of FIS is taken. The heat flow rate (in units of W) required to cause this mass loss is calculated as:

$$Q = L_f \Delta m \quad (13)$$

where $L_f = 3.34 \times 10^5 \text{ J kg}^{-1}$ is the latent heat of freezing. This yields a heat flow rate of around $Q = 0.15 \text{ TW}$. From this, the necessary temperature anomaly at MI_{lower} is calculated as:

$$\Delta T = \frac{Q}{c_p \rho_w \bar{u}_{P3} A} \quad (14)$$

where Q is the heat flow rate from equation (13), $c_p = 4,000 \text{ J kg}^{-1} \text{ K}^{-1}$ is the specific heat capacity of seawater, $\rho_w = 1,028 \text{ kg m}^{-3}$ is the density of seawater, $\bar{u}_{P3} = 3 \text{ cm s}^{-1}$ is the mean velocity into the cavity during P3 and $A = 6 \text{ km}^2$ is the area through which the inflow enters the cavity. A is estimated from a horizontal extent of 60 km and a vertical extent of 100 m. While 60 km is larger than the width of the sill at $M1_{\text{lower}}$, it is intended to also compensate the sill at $M3_{\text{lower}}$ and two additional sills without data west of $M1_{\text{lower}}$ (Fig. 1a). With these values, the result is a temperature difference of $\Delta T = 0.2 \text{ }^\circ\text{C}$.

Other data sources

All maps were created using the 'm_map' toolbox from ref. 82 and colormaps from ref. 83. Coastlines in Figs. 1a and 5c–e, and Extended Data Fig. 9 are from ref. 81; all other ones are from ref. 84. Grounding lines are from ref. 81. The satellite image of Antarctica shown in several figures was taken from ref. 73 and have been analysed in ref. 85.

Data availability

The FIS mooring data are available at <https://doi.org/10.21334/npolar.2023.4a6c36f5> ref. 74. Surface pressure, 10 m wind and 2 m air temperature are available from ERA5 at <https://doi.org/10.24381/cds.f17050d7> ref. 29. SIC and sea ice velocity are available from NSIDC at <https://doi.org/10.5067/8GQ8LZQVLOVL> ref. 30 and <https://doi.org/10.5067/INAWUW07QH7B> ref. 31, respectively. SSH is available upon request from ref. 32 and at <https://doi.org/10.17882/81032> ref. 86. The SAM index is available at <https://legacy.bas.ac.uk/met/gjma/sam.html> ref. 87. Data from mooring AWI253 are available at <https://doi.pangaea.de/10.1594/PANGAEA.875932> ref. 75 and <https://doi.pangaea.de/10.1594/PANGAEA.903315> ref. 76. Data for calculating basal melt rates from equation (6) are available at <https://doi.org/10.6075/J04Q7SHT> ref. 88.

Code availability

The MATLAB and Python scripts for data analysis and visualization can be obtained from the corresponding author upon reasonable request.

References

74. Lauber, J., de Steur, L., Hattermann, T. & Nøst, O. A. *Daily Averages of Physical Oceanography and Current Meter Data from Sub-Ice-Shelf Moorings M1, M2 and M3 at Fimbulisen, East Antarctica Since 2009* (Norwegian Polar Institute, 2023); <https://doi.org/10.21334/npolar.2023.4a6c36f5>
75. Schröder, M., Ryan, S. & Wisotzki, A. *Physical Oceanography and Current Meter Data from Mooring AWI253-1* (PANGAEA, 2017); <https://doi.org/10.1594/PANGAEA.875932>
76. Schröder, M., Ryan, S. & Wisotzki, A. *Physical Oceanography and Current Meter Data from Mooring AWI253-2* (PANGAEA, 2019); <https://doi.org/10.1594/PANGAEA.903315>
77. Martin, T., Tsamados, M., Schroeder, D. & Feltham, D. L. The impact of variable sea ice roughness on changes in Arctic Ocean surface stress: a model study. *J. Geophys. Res. Oceans* **121**, 1931–1952 (2016).
78. Dotto, T. S. et al. Variability of the Ross Gyre, Southern Ocean: drivers and responses revealed by satellite altimetry. *Geophys. Res. Lett.* **45**, 6195–6204 (2018).
79. Tsamados, M. et al. Impact of variable atmospheric and oceanic form drag on simulations of Arctic sea ice. *J. Phys. Oceanogr.* **44**, 1329–1353 (2014).
80. Student. The probable error of a mean. *Biometrika* **6**, 1–25 (1908).
81. Mouginot, J., Scheuchl, B. & Rignot, E. *MEaSURES Antarctic Boundaries for IPY 2007-2009 from Satellite Radar, Version 2* (NASA National Snow and Ice Data Center Distributed Active Archive Center, 2017); <https://doi.org/10.5067/AXE4121732AD>

82. Pawlowicz, R. M. *Map: A Mapping Package for MATLAB, Version 1.4m* www.eoas.ubc.ca/~rich/map.html (2020).
83. Thyng, K. M., Greene, C. A., Hetland, R. D., Zimmerle, H. M. & DiMarco, S. F. True colors of oceanography: guidelines for effective and accurate colormap selection. *Oceanography* **29**, 9–13 (2016).
84. Wessel, P. & Smith, W. H. F. A global, self-consistent, hierarchical, high-resolution shoreline database. *J. Geophys. Res.* **101**, 8741–8743 (1996).
85. Scambos, T. A., Haran, T. M., Fahnestock, M. A., Painter, T. H. & Bohlander, J. MODIS-based Mosaic of Antarctica (MOA) data sets: continent-wide surface morphology and snow grain size. *Remote Sens. Environ.* **111**, 242–257 (2007).
86. Auger, M., Prandi, P. & Sallée, J.-B. *Daily Southern Ocean Sea Level Anomaly and Geostrophic Currents from Multimission Altimetry, 2013-2019* (SEANOE, 2021); <https://doi.org/10.17882/81032>
87. Marshall, G. J. *An Observation-Based Southern Hemisphere Annular Mode Index* (British Antarctic Survey, 2023); <https://legacy.bas.ac.uk/met/gjma/sam.html>
88. Adusumilli, S., Fricker, H. A., Medley, B. C., Padman, L. & Siegfried, M. R. Data from: Interannual variations in meltwater input to the Southern Ocean from Antarctic ice shelves. *UC San Diego Library Digital Collections* <https://doi.org/10.6075/J04Q7SHT> (2020).

Acknowledgements

This research was funded by the Research Council of Norway through the KLIMAFORSK programme (iMelt, 295075). The installation of the moorings through the project 'ICE Fimbulisen - top to bottom' was financed by the Centre for Ice, Climate and Ecosystems (ICE), Norwegian Polar Institute (NPI). The moorings were maintained by NPI through ICE, the Norwegian Antarctic Research Expedition (IceRises 759, 3801-103) and iMelt. J.L. was funded by iMelt, T.H. and M.A. by the European Union's Horizon 2020 programme (CRiceS, 101003826 and SO-CHIC, 821001, respectively), and M.A. additionally by a CNES/CLS scholarship. The authors thank E. Schlosser for helpful discussions on SAM, and H. Goodwin, J. Kohler, S. Lidström and P. A. Dodd for help with fieldwork.

Author contributions

J.L. conducted the analyses, prepared the figures and wrote the initial manuscript with contributions from T.H., L.d.S. and E.D., who all supervised the work. M.A. provided SSH data and helped with their analysis. O.A.N. and T.H. installed the moorings, and O.A.N. assisted with analysing the circum-Antarctic changes. L.d.S. acquired funding (iMelt). G.M. advised on the interpretation of basal melt rates. All authors contributed to editing the manuscript.

Competing interests

The authors declare no competing interests.

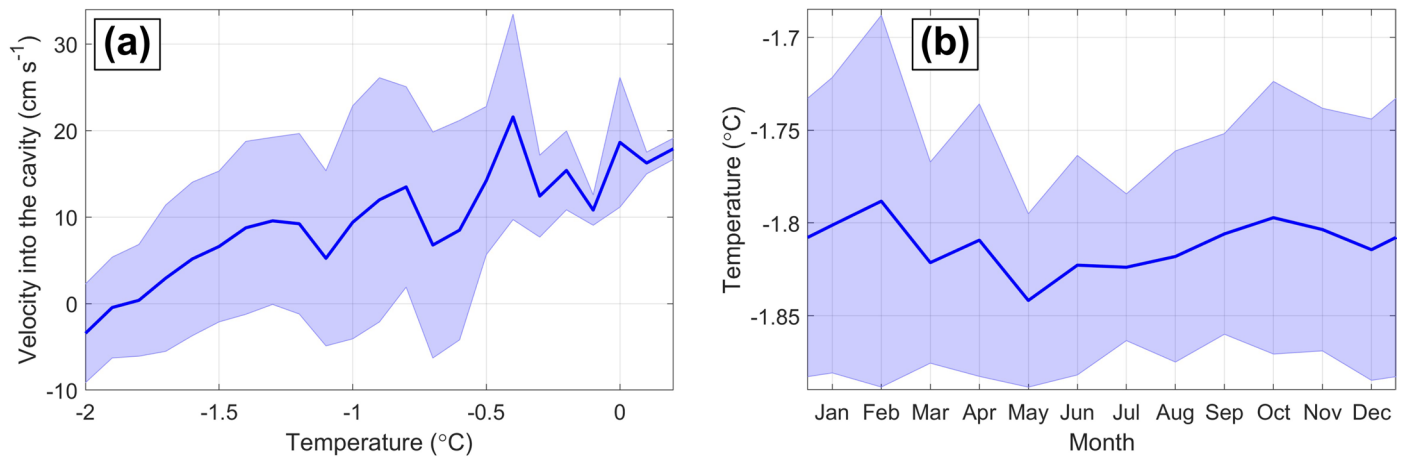
Additional information

Extended data is available for this paper at <https://doi.org/10.1038/s41561-023-01273-5>.

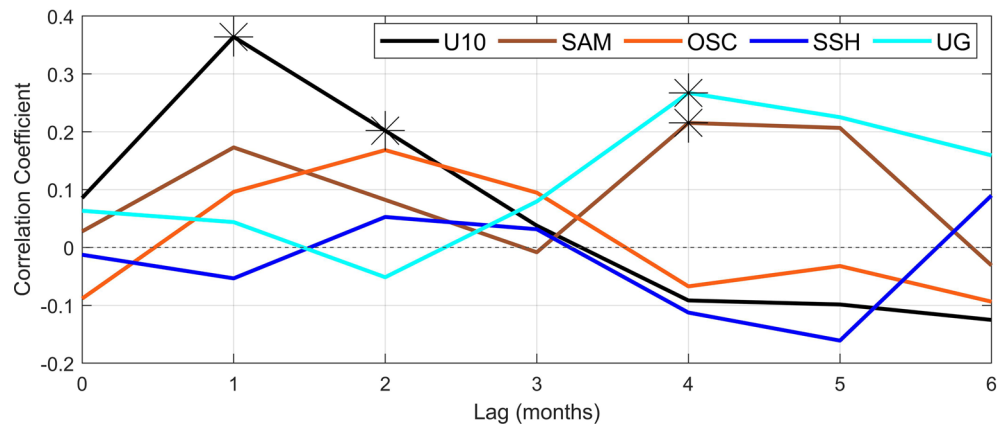
Correspondence and requests for materials should be addressed to Julius Lauber.

Peer review information *Nature Geoscience* thanks Madelaine Rosevear, Guy Williams and the other, anonymous, reviewer(s) for their contribution to the peer review of this work. Primary Handling Editor: Tom Richardson, in collaboration with the *Nature Geoscience* team.

Reprints and permissions information is available at www.nature.com/reprints.

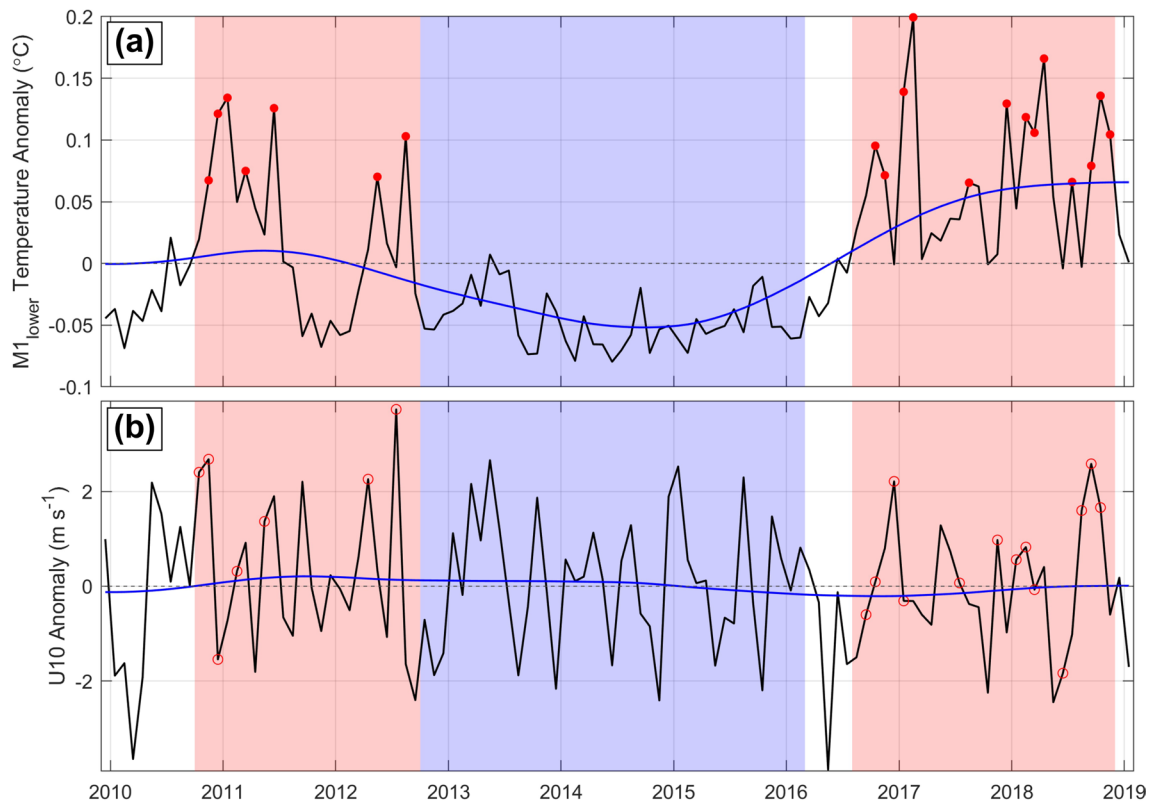


Extended Data Fig. 1 | Additional temperature and velocity analyses for MI_{lower} . **a**, Relation between temperature and velocity rotated into the cavity. Temperatures are binned into intervals of 0.1 °C, and all corresponding velocities are averaged and plotted against these bins. **b**, Monthly mean seasonal cycle of temperature. Envelopes in **a–b** mark the standard deviation.



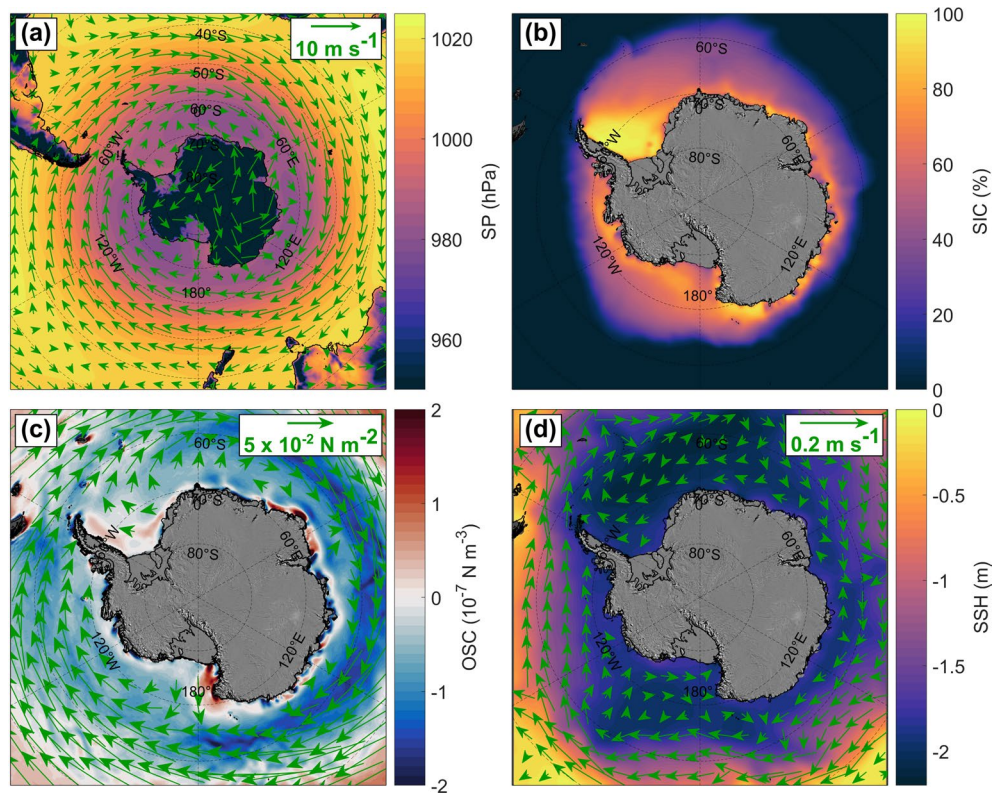
Extended Data Fig. 2 | Lagged correlation of $M1_{\text{lower}}$ temperature following selected forcing variables. U10 is the zonal 10 m wind, averaged over the same region as the time series in Fig. 3a. OSC is the ocean stress curl averaged over the same area. SAM is the Southern Annular Mode index, and SSH and UG are the

coastal sea surface height and zonal geostrophic velocity averaged over the areas from Fig. 3d–e. Correlations are calculated using de-seasoned, 48-month high-pass filtered time series. (same Method as in Fig. 1e–f). Stars indicate a significant correlation.

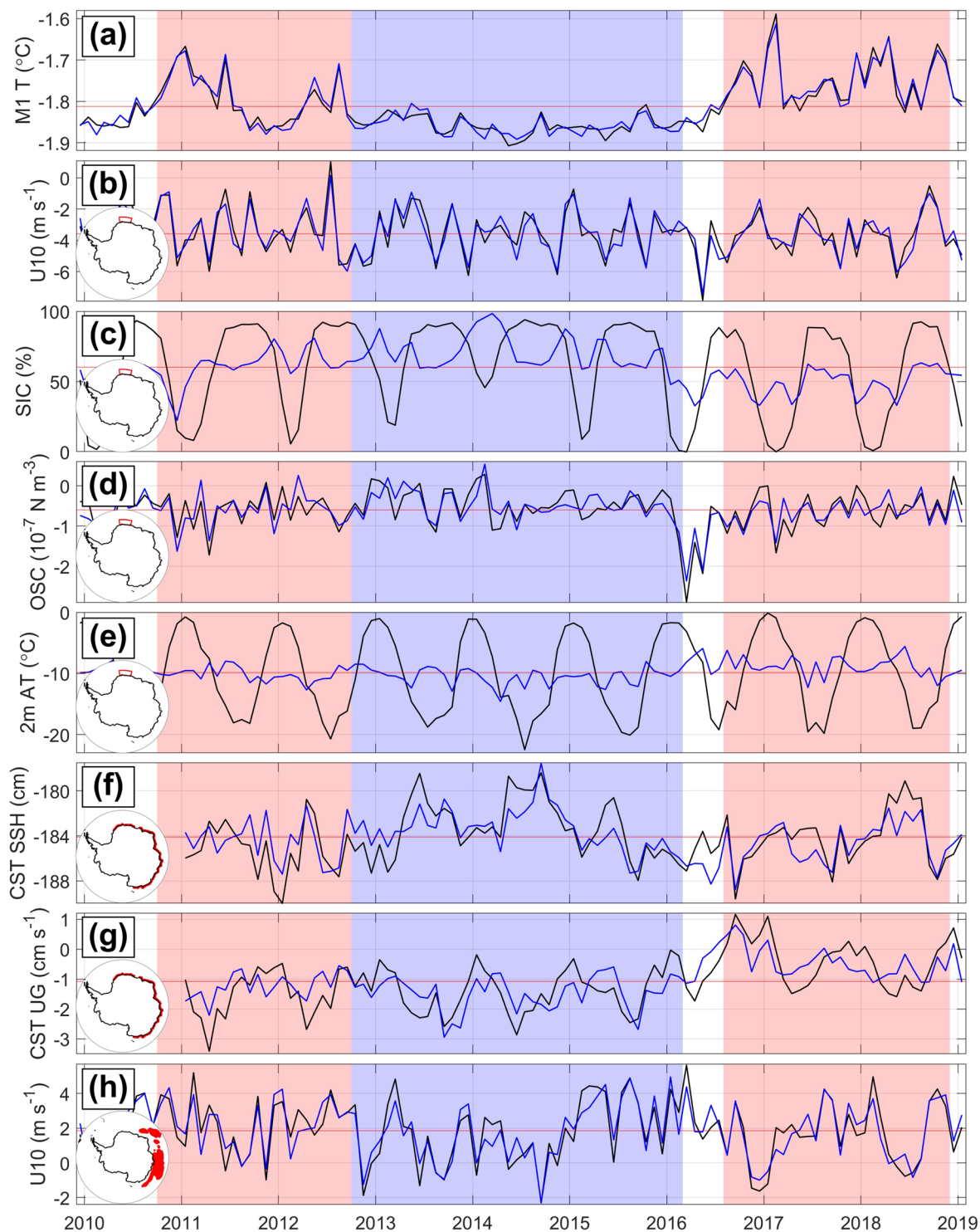
**Extended Data Fig. 3 | M1_{lower} temperature anomaly and local wind.**

a, De-seasoned M1_{lower} temperature. Red dots indicate months of warm inflow (same months as in Fig. 1c). **b**, Local zonal 10 m wind, averaged over the same

region as the time series in Fig. 3a. Red circles denote the months one month before each warm inflow event shown in a. Lines are monthly mean (black) and 48-month filtered (blue) time series. The color patches mark P1-3, as in Fig. 1c.

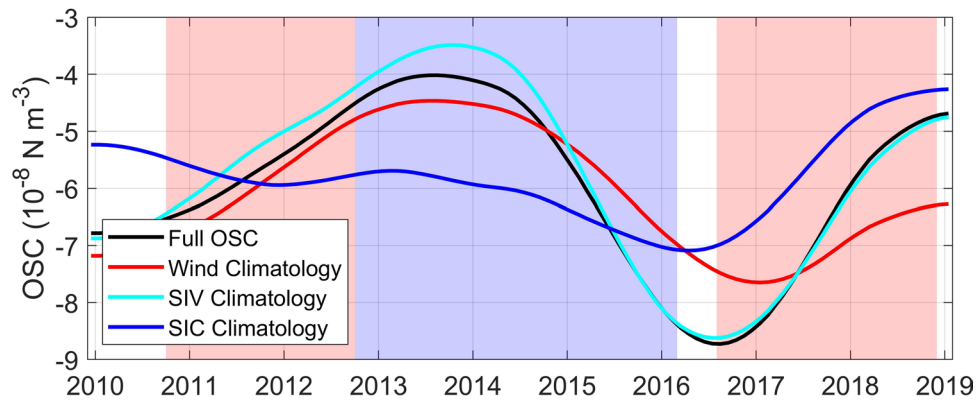


Extended Data Fig. 4 | Mean states of main auxiliary variables. a, 12/2009-01/2019 mean surface pressure (colors) and 10 m wind (arrows), **b**, 12/2009-01/2019 mean sea ice concentration, **c**, 12/2009-01/2019 mean ocean stress and its curl, **d**, 01/2011-12/2016 mean sea surface height and geostrophic currents. The satellite image in **b–d** is from ref. 73.

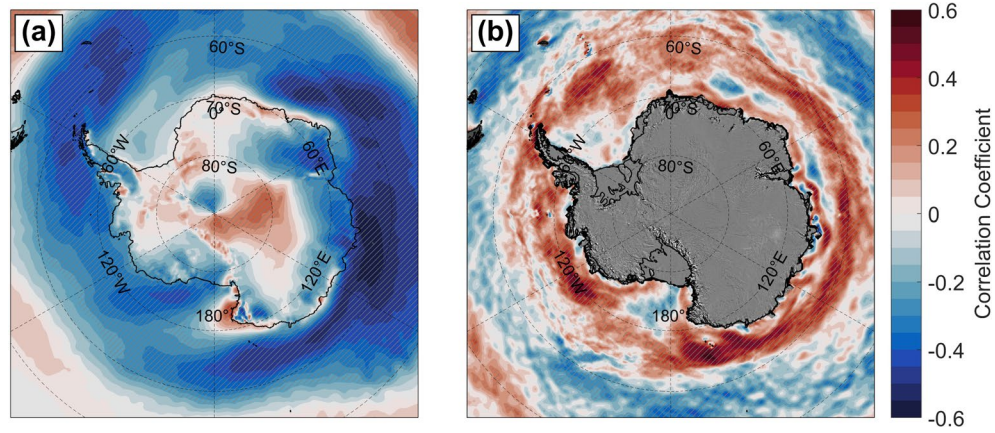


Extended Data Fig. 5 | Comparison between absolute (black) and de-seasoned (blue) variables. a, $M1_{\text{lower}}$ temperature, b, local zonal 10 m wind, c, sea ice concentration, d, ocean stress curl, e, 2 m air temperature, f, coastal sea surface height, g, coastal zonal geostrophic velocity, h, East-Antarctic subpolar zonal

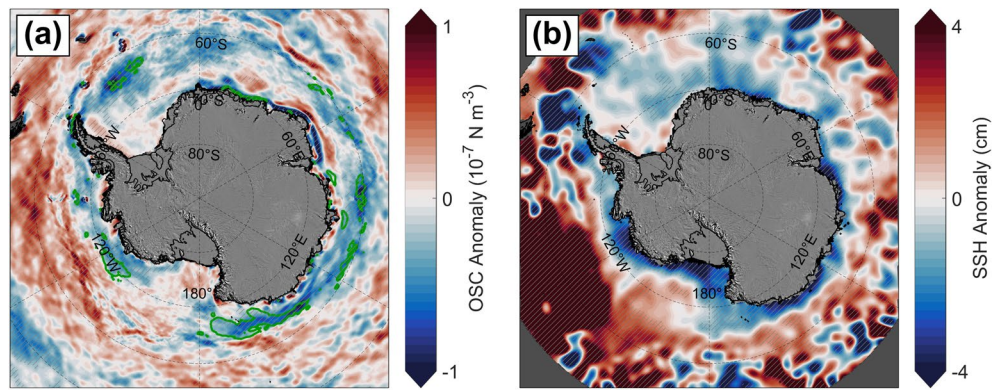
wind. The time series have been averaged over the same areas as in Fig. 3 and Extended Data Fig. 3b. For better comparability, the time mean of the absolute values has been added to the de-seasoned time series.



Extended Data Fig. 6 | Effects of wind and sea ice on the ocean stress curl variability. The black curve is the full ocean stress curl averaged as in Fig. 3b. The colored curves are versions of the ocean stress curl where either wind, sea ice velocity, or sea ice concentration are replaced by seasonally averaged values and thus do not contain any interannual variability.

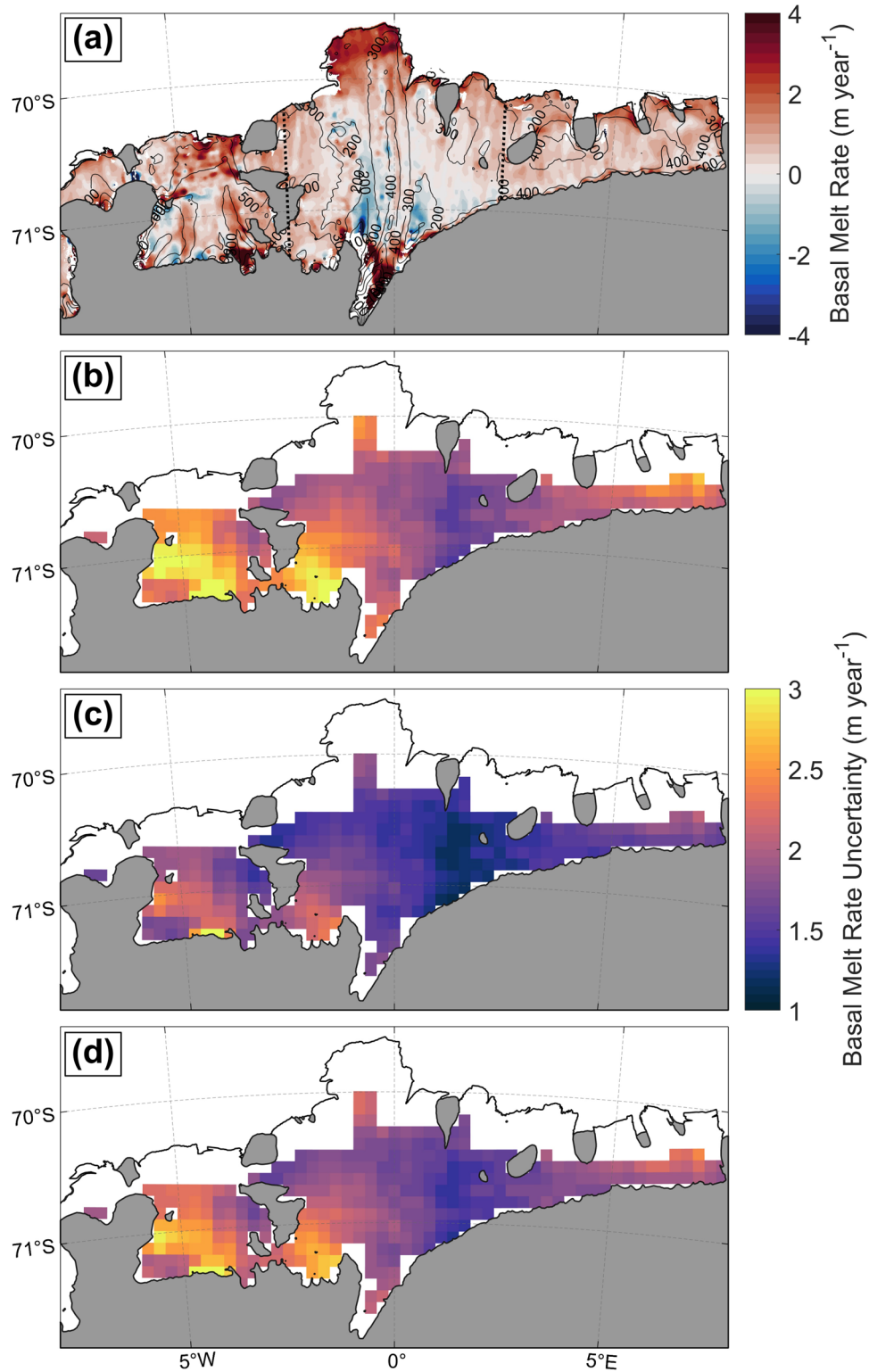


Extended Data Fig. 7 | Correlations of coastal sea surface height and zonal wind or ocean stress curl. a, Spatial correlation between the de-seasoned coastal sea surface height from Fig. 3d and the de-seasoned zonal 10 m wind. **b**, Same as a, but for ocean stress curl instead of zonal 10 m wind. The satellite image in **b** is from ref. 73.



Extended Data Fig. 8 | Changes in forcing from P2 to P3. a, Difference in de-seasoned ocean stress curl between 01/2015-01/2017 and 01/2013-12/2014 (orange and cyan bars in Fig. 3a). The green contour marks the areas where the

correlation of the coastal sea surface height (Fig. 3d) and the ocean stress curl is at least 0.4 (see Extended Data Fig. 7b). Hatched areas indicate significance. **b,** Same as **a**, but for sea surface height. Satellite image from ref. 73.



Extended Data Fig. 9 | Mean basal melt rate and uncertainty during P1-3 at Fimbulisen. a, 2010 to 2018 average. The black contours indicate the ice shelf draft in meters. Two thick dotted black lines mark 2.5°W and 2.5°E, which were

used as bounding longitudes for mass balance estimates (see Methods). **b-d**, Uncertainty for the P1-3 average shown in Fig. 5c-e, calculated with data from Adusumilli et al. (³⁵ see Methods).